Dendrite tapering actuates a self-organizing signaling circuit for stochastic filopodia initiation in neurons

Gloria Mancinelli[a,b], Lucas Lamparter[a,b], Georgii Nosov[a,b], Tanumoy Saha[a,b], Anna Pawluchin[a,b], Rainer Kurre[c], Christiane Rasch[a], Mirsana Ebrahimkutty[a,b], Jürgen Klingauf[a,b], and Milos Galic[a,b,1]

[a]Institute of Medical Physics and Biophysics, University of Münster, 48149 Münster, Germany; [b]Cells in Motion Interfaculty Center, University of Münster, 48149 Münster, Germany; and [c]CellNanOS, Osnabrück University, 49076 Osnabrück, Germany

Edited by Jennifer Lippincott-Schwartz, Janelia Farm Research Campus, Ashburn, VA, and approved September 1, 2021 (received for review April 12, 2021)

How signaling units spontaneously arise from a noisy cellular background is not well understood. Here, we show that stochastic membrane deformations can nucleate exploratory dendritic filopodia, dynamic actin-rich structures used by neurons to sample its surroundings for compatible transcellular contacts. A theoretical analysis demonstrates that corecruitment of positive and negative curvature-sensitive proteins to deformed membranes minimizes the free energy of the system, allowing the formation of long-lived curved membrane sections from stochastic membrane fluctuations. Quantitative experiments show that once recruited, curvature-sensitive proteins form a signaling circuit composed of interlinked positive and negative actin-regulatory feedback loops. As the positive but not the negative feedback loop can sense the dendrite diameter, this self-organizing circuit determines filopodia initiation frequency along tapering dendrites. Together, our findings identify a receptor-independent signaling circuit that employs random membrane deformations to simultaneously elicit and limit formation of exploratory filopodia to distal dendritic sites of developing neurons.

membrane curvature | self-organization | BAR domain | filopodia | neuron

A crucial first step toward a functional neuronal network is to establish contact with the correct synaptic partners. To accomplish this daunting task, individual neurons undergo a phase of intense transcellular sampling (1, 2). To augment the sampling volume, and thus the total number of possible encounters, neurons rely on actin-rich exploratory filopodia that form along dendritic arbors (1, 3–5). From this overabundance of transcellular contacts, only connections with compatible surface identities mature into synapses (6), while mismatched interfaces are rapidly aborted (1, 2).

Seminal work over the past decades has elucidated the machinery driving filopodial dynamics in neuronal and non-neuronal cells. These studies established an intricate signaling network that regulates actin polymerization during filopodial growth and retraction. In addition, several extra- and intracellular signaling cues have been identified that trigger filopodia formation (7–9). Yet, given its exploratory purpose and that sampling behavior is not only observed in brain slices (2) but also in sparsely cultured neurons that lack neighbors (1), suggests that filopodial initiation also occurs in the absence of causative signaling cues. Indeed, stochastic membrane deformations induced by actin polymerization were described to initiate finger-like protrusions reminiscent of filopodia in vitro (10–12). Similarly, filopodia emerge at lamellipodia from cone-shaped precursors in cells (13), establishing membrane curvature as central element at the onset of filopodial formation. If and how cells utilize membrane geometry to control filopodia initiation in neurons, however, is not fully understood.

Combining quantitative light and electron microscopy of primary hippocampal neurons with chemical approaches and computational modeling, we find that binding of curvature-sensitive proteins alters the lifetime of stochastically deformed membrane sections. Intriguingly, these proteins not only enrich at nascent filopodia but also alter local polymerization dynamics. This dual ability to sense and induce membrane deformations is relevant, as it allows the formation of a self-organizing signaling circuit. As this circuit is curvature sensitive, dendrite tapering augments exploratory filopodia initiation at thin, distal ends. Our results present a receptor-independent mechanism used by neurons to nucleate signaling hubs and facilitate transcellular sampling in a curvature-dependent fashion.

Results

Dendritic Tapering Increases Filopodial Initiation Frequency and the Concentration of Negative Curvature-Sensing Proteins. To assess filopodial growth dynamics, we performed live-cell microscopy in fluorescently labeled primary hippocampal neurons on day in vitro 7 to 9 (Fig. 1*A*). Consistent with published work (1, 14, 15), exploratory dendritic filopodia formed at a rate of 0.05 protrusions per 15 min along a stretch of 10-μm length (Fig. 1*B* and *SI Appendix*, Fig. S1*A*). Strikingly, we find a strong bias for filopodial initiation events toward small-diameter dendrites (Fig. 1*B*), which are mainly present at distal ends (Fig. 1*C*), raising the possibility that membrane curvature along the transverse dendritic plane (i.e., perpendicular to principal dendrite axis) may affect exploratory behavior. Indeed, several negative

Significance

Cellular signaling pathways respond to a wide range of stimuli. How signaling circuits are activated without an instructive stimulus and what this is good for are less clear. Combining theoretical and experimental approaches, we show that curvature-sensing proteins stabilize stochastic membrane deformations to nucleate a self-organizing actin-regulatory signaling circuit. In neurons, these signaling hubs control the initiation of exploratory filopodia that sample the cell vicinity for appropriate synaptic partners. The extent and diversity of proteins capable of forming self-organizing circuits at stochastically deformed membranes indicates a general signaling mechanism.

Author contributions: G.M., L.L., G.N., T.S., A.P., R.K., C.R., M.E., J.K., and M.G. designed research; G.M., L.L., G.N., T.S., A.P., R.K., C.R., M.E., and M.G. performed research; G.M., L.L., G.N., T.S., A.P., R.K., C.R., M.E., J.K., and M.G. analyzed data; and G.M., L.L., and M.G. wrote the paper.

The authors declare no competing interest.

This article is a PNAS Direct Submission.

[1]To whom correspondence may be addressed. Email: galic@uni-muenster.de.

This article contains supporting information online at http://www.pnas.org/lookup/suppl/doi:10.1073/pnas.2106921118/-/DCSupplemental.

Published October 22, 2021.

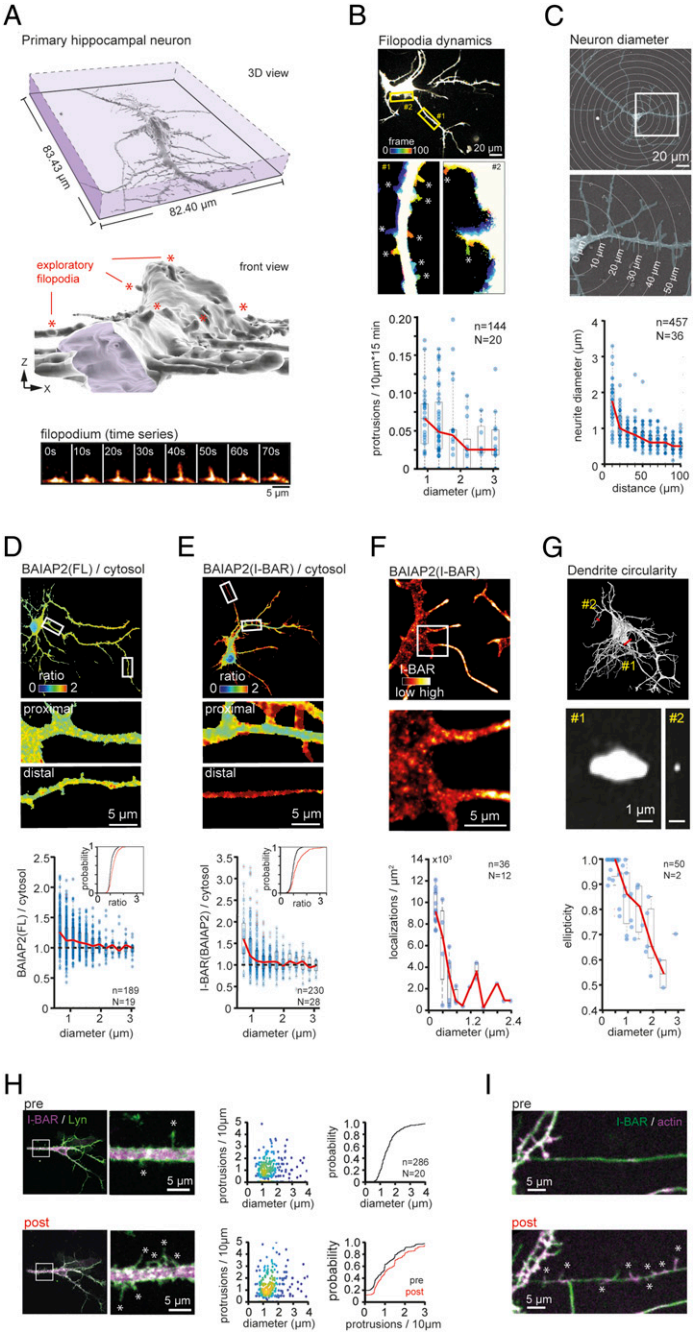

Fig. 1. Membrane curvature, filopodial initiation frequency, and BAIAP2 protein concentration increase toward distal dendritic ends. (*A*) Lattice light-sheet image of primary hippocampal neuron at DIV9 depicted from bird's-eye (*Top*) and front (*Middle*) view. Individual exploratory filopodia are labeled with red asterisk. Time series of a representative filopodial extension–retraction cycle is shown below. (Scale bar, 5 µm.) (*B*) Filopodia initiation frequency increases in dendrites with small diameter. Neurons were transfected at DIV7 and imaged 24 h later. Color-coded time series of neuron imaged at 1 Hz (*Top*) and statistical analysis (*Bottom*) is shown (n = 144 neurites from n = 20 cells). (Scale bar, 20 µm.) (*C*) Dendrites narrow toward the distal end. SEM image and quantification (n = 457 neurites from n = 36 cells) of DIV9 neuron are shown. (Scale bar, 20 µm.) (*D*) Curvature-dependent enrichment of BAIAP2 in thin dendritic sections. (*Top*) Ratiometric analysis of neuron cotransfected with YFP-BAIAP2 and an empty mCherry plasmid as cytosolic reference is shown. Analysis of curvature-dependent enrichment and corresponding cumulative distribution (*Inset*) are shown below (n = 189 neurites from n = 19 cells; $P = 1.50 \times 10^{-18}$ after Mann–Whitney U test [MW]). (Scale bar, 5 µm.) (*E*) Enrichment of curvature-sensitive I-BAR domain of BAIAP2 in thin dendrite sections. Neurons were cotransfected with negative (i.e., outward) curvature-sensing I-BAR domain of BAIAP2 and a cytosolic reference. Analysis is shown below (n = 230 neurites from n = 28 cells; $P = 3.99\ 10^{-21}$ after MW). (Scale bar, 5 µm.) (*F*) TIRF-PALM quantification of curvature-dependent enrichment of I-BAR domain of BAIAP2 in thin dendritic regions (n = 36 neurites from n = 12 cells). (Scale bar, 5 µm.) (*G*) Lattice light-sheet microscopy indicates flattening of thick proximal dendritic sections along the z-axis (n = 50 neurites from n = 2 cells). (Scale bar, 1 µm.) (*H*) Induced membrane curvature triggers filopodia formation. (*Left*) Cells expressing membrane-associated FRB-Lyn and FBKP-IBAR-YFP are shown before (*Top*) and after (*Bottom*) addition of rapamycin. Neurons were transfected at DIV7 and imaged 24 h later (pre = 15 min before, post = 25 min after 100 nM rapamycin was added). Note that addition of rapamycin causes enrichment of FKBP-IBAR-YFP at the plasma membrane. Next to it, analysis of filopodia density as function of the dendrite diameter, as well as cumulative distribution of dendrite diameter (*Right*, *Top*) and protrusion density (*Right*, *Bottom*) (n = 286 neurites from n = 20 cells). (Scale bar, 5 µm.) (*I*) Rapamycin-induced membrane deformation triggers formation of actin-rich filopodia (asterisk). Dendritic sites are shown prior (*Top*) and after (*Bottom*) addition of rapamycin. Note the formation of actin-rich (magenta) filopodia. (Scale bar, 5 µm.)

(i.e., outward) curvature-sensing proteins, namely MTSS1 (i.e., MIM) (16), MTSS2 (i.e., ABBA) (17), and BAIAP2 (i.e., IRSP53) (18), were described to regulate filopodia and spine formation in neurons. MTSS1, an Arp2/3 promotor and Formin inhibitor, facilitates dendritic spine initiation in hippocampal neurons (16) and spine shape changes in dendritic cells (19). Similarly, the exercise-induced protein MTSS2 (17) and the scaffolding/adaptor protein BAIAP2 (18) both promote dendritic protrusion in cultured hippocampal neurons. Consistent with curvature-dependent recruitment, these proteins enrich in filopodia (16, 20) and the leading edge (21–23). If dendrite tapering may influence localization of these proteins, however, it has not been addressed thus far.

As BAIAP2 displayed the most selective expression in hippocampal neurons (24), we proceeded with this prototypic negative curvature-sensing protein. To that end, we expressed fluorescently labeled BAIAP2 together with an empty mCherry plasmid as cytosolic reference. In line with in vitro studies that show BAIAP2 enrichment in membrane tethers (25), we observe augmented BAIAP2 levels in highly curved dendritic sections (Fig. 1*D*). No BAIAP2 enrichment was observed at flat membrane sections of the soma (*SI Appendix*, Fig. S1 *B* and *C*). To exclude the possibility that curvature-dependent BAIAP2 recruitment was caused by other protein domains, and to eliminate the autoinhibited cytosolic fraction (26), we probed the subcellular localization of the isolated I-BAR domain. Strikingly, we find accumulation of the negative curvature-sensitive I-BAR domain of BAIAP2 in small-diameter dendrites (Fig. 1*E*). As above, no enrichment was observed at flat membranes (*SI Appendix*, Fig. S1*D*). To further validate these findings, we performed photoactivated localization microscopy (PALM) superresolution microscopy. Using the evanescent wave of a total internal reflection fluorescence (TIRF) microscope, we selectively illuminated membrane-associated events. Consistent with our previous results, we measure increased concentration of the I-BAR domain of BAIAP2 in highly curved dendritic membrane sections (Fig. 1*F* and *SI Appendix*, Fig. S1 *E* and *F*). Curiously, confocal and TIRF-PALM images displayed protein enrichment in some proximal dendrite sections. We thus analyzed the cell volume using lattice light-sheet microscopy. For dendrites with large diameter, we find flattening along the *z*-axis (Fig. 1*G*), likely providing additional binding sites for curvature-sensitive proteins at proximal regions of neurons cultured on glass slides.

Importantly, the isolated I-BAR domains of MTSS1 and MTSS2 also enriched in narrow dendrites (*SI Appendix*, Fig. S2 *A* and *B*). The same was true for the inverse F-BAR (iF-BAR) domains of SRGAP2 and SRGAP3 (*SI Appendix*, Fig. S2 *C* and *D*), arguing that negative membrane curvature and not protein identity cause protein recruitment. Consistently, the positive curvature-sensing N-BAR domains of ARHGAP44, AMPH1, AMPH2, ENDO1, and NADRIN1 did not enrich at highly curved dendritic sites (*SI Appendix*, Fig. S2 *E–I*). Similarly, no curvature-dependent enrichment was observed for the planar membrane promoting PINKBAR domain (27) (*SI Appendix*, Fig. S2*I*) or the positive curvature-sensing F-BAR domains of CIP4 and FCHO2 (*SI Appendix*, Fig. S2 *K* and *L*). The F-BAR domain of FCHO1 enriched at distal ends and displayed patch-like protrusions along dendrites (*SI Appendix*, Fig. S2*M*).

Our data shows that protein concentrations and protrusion dynamics both change in a curvature-dependent manner, raising the possibility that these observations may be functionally connected. BAIAP2 forms autoinhibited cytosolic dimers, which display concentration-dependent interactions with filopodia-promoting proteins (8, 28). Similar to other actin-regulatory proteins (29, 30), activation of this protein relies on coincidence detection (8). Considering that the protein readily transitions between active and autoinhibited state (26), we reasoned that membrane curvature may promote filopodia formation by mediating the active membrane-bound state of BAIAP2 (*SI Appendix, Supplementary Information Text*). Taking advantage of a chemical dimerization assay (31, 32), we induced artificial membrane deformations and monitored its effect on filopodia density (*SI Appendix*, Fig. S2 *N* and *O*). We observed an acute increase in dendritic protrusions upon dimerization (Fig. 1*H*). Since massive overexpression of the sole BAR domain has been described to form actin-free protrusions (26), we probed for the presence of actin in these newly formed structures. We find newly formed protrusions to be filled with actin (Fig. 1*I*), indicative of a curvature-dependent initiation of exploratory dendritic filopodia.

Protein–Membrane Interactions Minimize the Free Energy and Prolong the Lifetime of Curved Membrane Sections. The findings thus far show that curvature-dependent protein enrichment positively correlates with filopodial formation. It does, however, not answer the question what triggers initiation of these actin-rich structures in the first place. Several receptor-based signals have been reported to mediate formation of dendritic filopodia in neurons (9, 33). Since the exploratory stage not only temporally precedes functional synaptic terminals but also occurs in sparsely cultured neurons without neighbors that may provide signaling cues, this argues for a stochastic rather than a receptor-based mechanism for exploratory filopodia initiation.

How could curved membrane sections, which nucleate filopodia formation, form in the absence of an instructive signal? From an energy standpoint, a membrane with homogeneously mixed lipids is unlikely to remain bent over an extended period of time (Fig. 2*A*, black), unless a constant force is applied (34). In theory, lipid phase separation may yield membrane deformations that trigger curvature-dependent protein recruitment (35). Such lipid patches, however, are long lived and thus not well suited for a stochastic sampling mechanism. Intriguingly, the minimal free energy state of a membrane shifts upon binding of curvature-sensitive proteins (Fig. 2*A*, red). To probe the relevance of curvature-dependent protein–membrane interactions, we explored the energy landscape of such a system. Consistent with previous reports (25, 36, 37), we employed a curvature mismatch model (for details reference *SI Appendix, Supplementary Information Text*). Here, the equilibrium protein saturation can be obtained by minimizing the free energy with respect to the fraction of the membrane area covered by curvature-sensitive proteins. We find the minimal free energy state of a membrane/protein system to approximate a uniformly curved membrane, whereby protein concentration and mean curvature positively correlate (Fig. 2*B* and *SI Appendix*, Fig. S3*A*).

To further investigate these theoretical energy considerations, we used the Gillespie algorithm to develop a stochastic two-dimensional (2D) Monte Carlo model of curvature-dependent protein–membrane interactions (for details reference *SI Appendix, Supplementary Information Text*). For simplicity and robustness, we deliberately used a reductionist model depicting the membrane as a line that is divided into sections of 50-nm length. In each time step, one of four events can happen at every membrane patch: 1) a protein binds to the membrane, 2) a protein unbinds from the membrane, 3) the membrane patch moves up, or 4) the membrane patch moves down. The probability of each event is given by its individual reaction (i.e., transition) rates. Consistent with the theoretical energy considerations, increasing protein levels in this stochastic numerical model positively correlated with the final membrane (i.e., line) curvature (Fig. 2*C*). In all cases, the membrane fluctuated around a particular uniform global curvature (Fig. 2*D* and Movie S1). In accordance with previously published experimental (38) and theoretical (39) work, lowering membrane rigidity in the presence of negative curvature-sensitive proteins led to the rapid formation of tubular structures (*SI Appendix*, Fig. S3*B*).

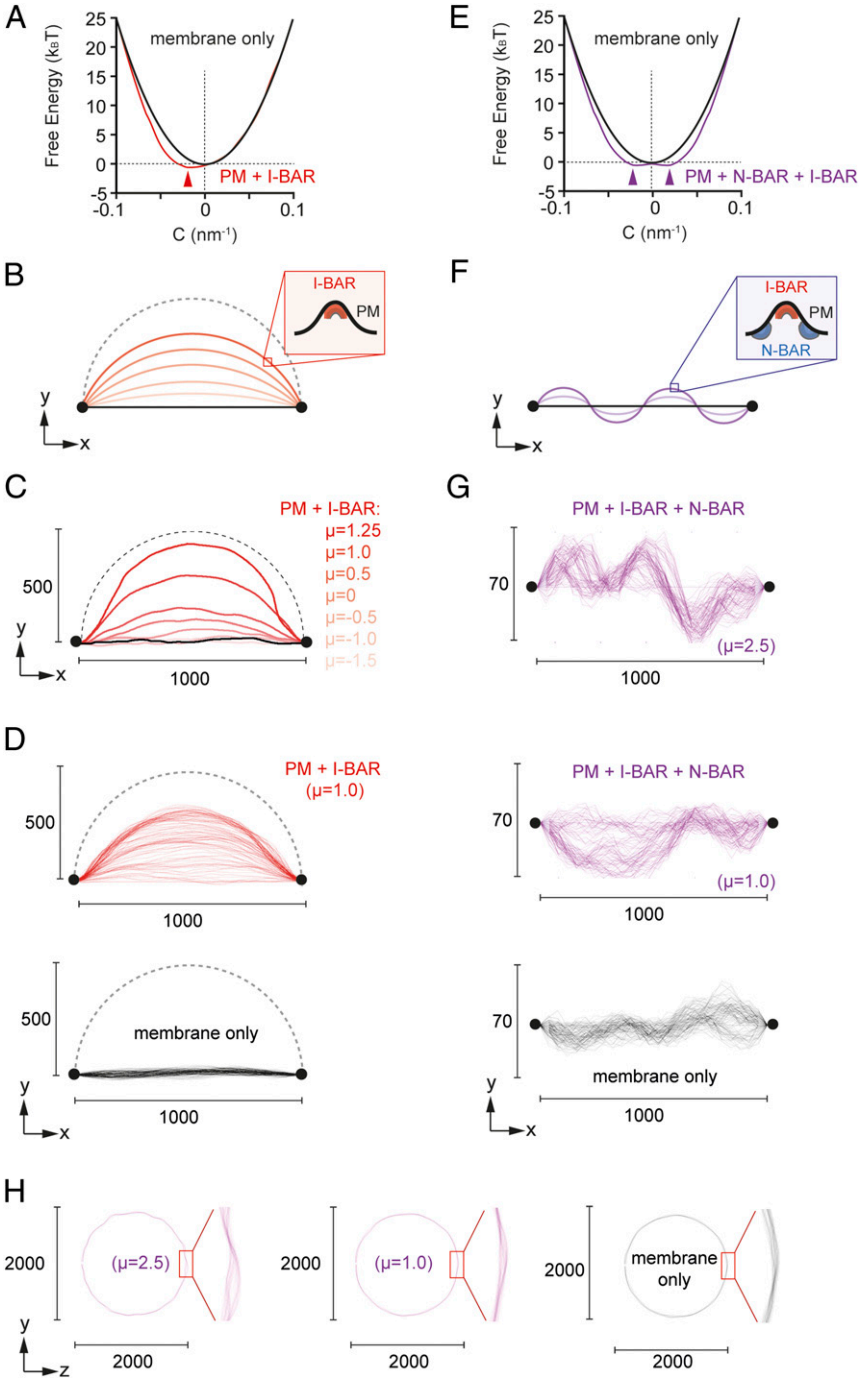

Fig. 2. Energy considerations of membrane geometry upon binding of curvature-sensing proteins. (*A*) The minimal energy state of a membrane is at zero curvature (black). Upon membrane binding of curvature-sensitive proteins (red), the minimal energy state is a curved membrane. (*B*) To minimize the free energy of the system, a membrane displays a uniformly curved shape upon binding of curvature-sensitive proteins. Note that final curvature depends on protein concentration (darker red = higher protein concentration). (*C*) End point of Monte Carlo simulation depicting membrane alone (black) or a system consisting of the membrane and a negative curvature-sensitive protein (red). Note concentration-dependent increase of membrane curvature in the presence of the negative curvature-sensitive protein (settings: time = 5,000, membrane rigidity = 50, I-BAR rigidity = 35, I-BAR curvature = -1/20, I-BAR concentration μ is displayed in figure). (*D*) Time series of initial 5,000 time steps of linear Monte Carlo simulation in the presence (red) and absence (black) of curvature-sensitive protein (settings: time = 5,000, time increment = 50, membrane rigidity = 50, I-BAR rigidity = 35, I-BAR curvature = -1/20, I-BAR μ = 1.0). (*E*) A system consisting of two proteins with opposite curvature preference displays two local minima. Sole membrane (black) and system consisting of membrane and two proteins with opposing curvature preference (purple) are shown. (*F*) In a system that consists of two curvature-sensitive proteins with opposing curvature selectivity, the minimal energy state is an undulating membrane. (*G*) Time series of Monte Carlo simulation of linear membrane in the absence (black) or in the presence (purple) of different protein concentrations (settings: time = 5,000, time increment = 50, membrane rigidity = 50, I-BAR rigidity = 35, N-BAR rigidity = 35, I-BAR curvature = -1/20, N-BAR curvature = 1/20, μ of I-BAR and N-BAR is displayed in figure). (*H*) Initial 300 time steps of circular Monte Carlo simulation in the presence (purple) and absence (black) of curvature-sensitive proteins (settings: time = 300, time increments = 3, membrane rigidity = 50, I-BAR rigidity = 35, N-BAR rigidity = 35, I-BAR curvature = -1/20, N-BAR curvature = 1/20, μ of I-BAR and N-BAR is displayed in figure). Note that the numerical model depicts membrane length in nanometers and time steps in seconds. The corresponding simulation parameters can be found in *SI Appendix, Supplementary Information Text*.

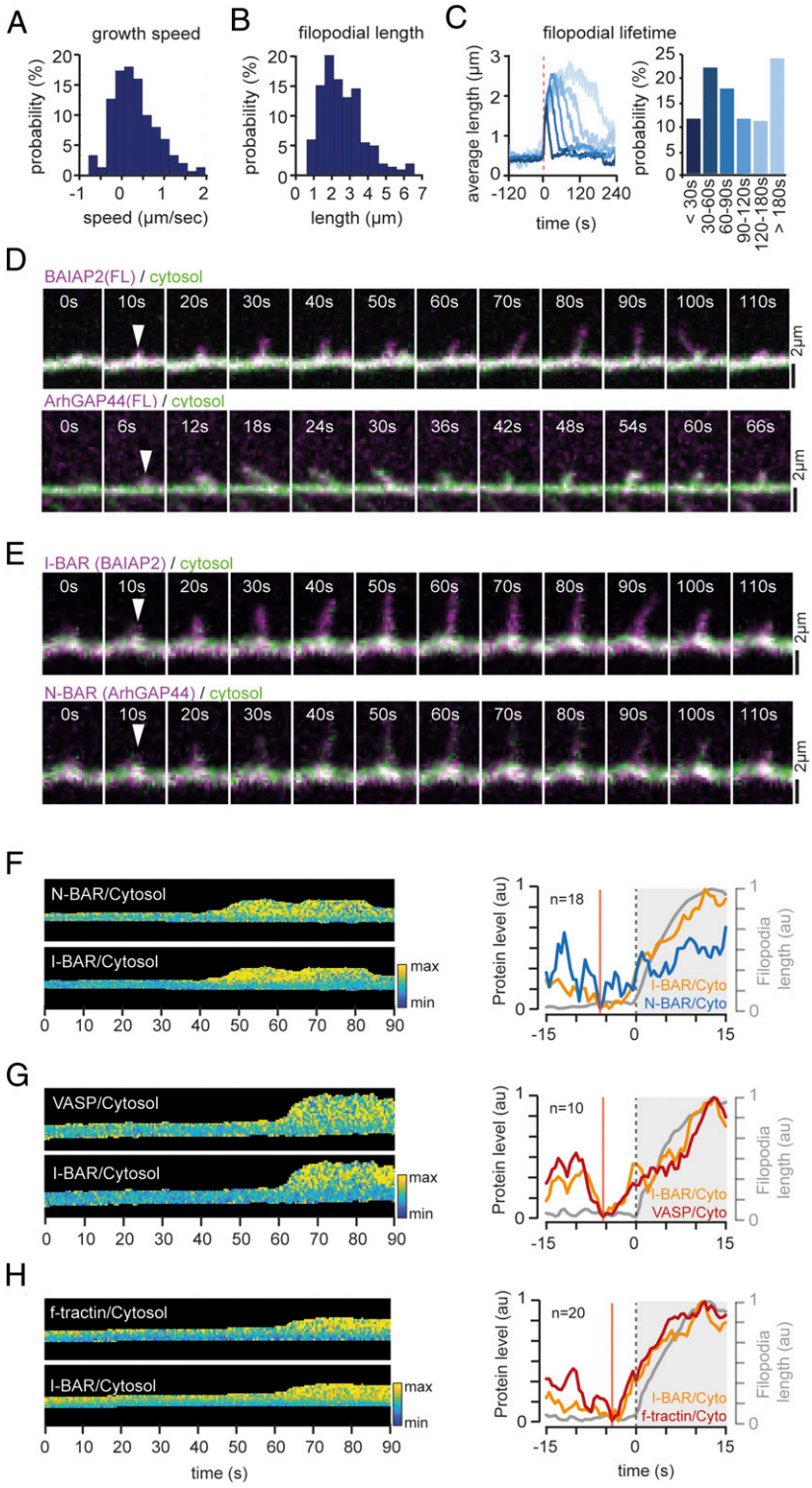

Fig. 3. Negative and positive curvature-sensitive proteins coenrich in neurons at nascent filopodial sites. (*A*) Analysis of initial filopodial growth speed. For quantification, the growth in the first 2 s after reaching 25% of the maximal length was measured (n = 150 filopodia, n = 20 neurons). (*B*) Quantification of average filopodial length (n = 204 filopodia, n = 30 neurons). (*C*) Extension–retraction dynamics of individual filopodia grouped by lifetime (n = 204 filopodia, n = 30 neurons). (*D*) BAIAP2 and ARHGAP44 both enrich at nascent filopodial sites prior to elongation. Cells were transfected with the full-length protein (magenta) and a cytosolic reference (green). Note enrichment of BAIAP2 (*Top*) and ARHGAP44 (*Bottom*) prior to elongation (arrow). (*E*) The BAR domains of BAIAP2 and ARHGAP44 both enrich at nascent filopodial sites prior to elongation. Cells were transfected with the respective BAR domain (magenta) and a cytosolic reference (green). Note enrichment of I-BAR domain of BAIAP2 (*Top*) and the N-BAR domain of ARHGAP44 (*Bottom*) prior to elongation (arrow). (*F*) Color-coded ratiometric kymographs of the N-BAR domain of ARHGAP44 over cytosolic reference (*Top*) and the I-BAR domain of BAIAP2 over cytosol (*Bottom*). Pixel size of kymograph: x-axis = 0.5 s, y-axis = 0.2 μm. Quantification is shown to the *Right* (n = 18 filopodia). Note enrichment of both biosensors prior to extension. (*G*) Ratiometric analysis shows coenrichment of VASP and I-BAR domain prior to filopodial extension (n = 10 filopodia). (*H*) Ratiometric analysis shows coenrichment of actin and I-BAR domain prior to filopodial extension. As above, an exemplary kymograph and averaged values are presented (n = 20 filopodia).

While such a system favors curvature in one direction, it displays a strong energy penalty for membrane deformation in the opposite directions. To form undulating structures at physiological protein concentration and membrane rigidity, which can be observed at nascent filopodial sites (40), we reasoned that a system consisting of positive and negative membrane deforming agents may be better suited (Fig. 2*E*). To test this hypothesis, we expanded the curvature mismatch model, adding a second protein that binds to membrane deformations in the opposite direction. With increasing protein concentrations, the free energy minimum of this expanded system first widened, upon which two separate local minima for positively and negatively curved membranes formed (Fig. 2*F*). Consistently, the corresponding expanded Monte Carlo model led to local membrane deformations in both directions. This was true for both a linear 2D system (Fig. 2*G* and Movie S2 and *SI Appendix*, Fig. S3 *C–F*) as well as for a circular 2D system with constant negative curvature (Fig. 2*G* and Movie S3). Intriguingly, at intermediate protein concentrations both two-component systems transitioned between various highly curved metastable states (Fig. 2 *E* and *F* and Movies S2 and S3). This is relevant, as it suggests that in the presence of two opposing curvature-sensitive proteins the lifetime and amplitude of transient membrane deformations increase. Considering that cellular membranes are continuously deformed by active and thermal processes (41), and that curved membrane sections modulate the actin velocity field (10) and induce actin bundling (12), stabilization of stochastically deformed local membrane sections via curvature-sensitive proteins are likely to augment filopodia initiation probability.

Curvature-Dependent Signaling Circuits Determine Transcellular Sampling in Neurons. To experimentally probe the model predictions, we used an adaptive filopodia tracking software (42) to analyze 204 individual filopodia initiation events in primary hippocampal neurons. In line with an exploratory function, the majority of filopodial protrusions rapidly grew to a median length of 2.38 μm (Fig. 3 *A* and *B*) and then collapsed (Fig. 3*C*). Filopodia with a lifetime smaller than 2 min showed a positive correlation for lifetime and length but no apparent differences in growth speed (Fig. 3*C*). Consistent with published work (43), the observed growth rate was maximal just after initiation and declined thereafter (Fig. 3*C*).

Having established a quantitative analysis platform for filopodial initiation, we then probed whether curvature-sensitive proteins with opposing curvature preference coenrich at nascent filopodia. A literature search identified 19 curvature-sensing actin regulators, 7 of which (i.e., BAIAP2, MTSS1, MTSS2, ARHGAP44, SRGAP1, SRGAP2, and SRGAP3) are predominantly expressed in the central nervous system (*SI Appendix*, Fig. S4). Among these, only ARHGAP44 (i.e., RICH2, NADRIN2) is sensitive for positive membrane deformations. We therefore proceeded with BAIAP2 and ARHGAP44. Consistent with model predictions (Fig. 2*H*), both curvature-sensing proteins enriched at nascent filopodial sites prior to extension (Fig. 3*D*). The same was true for the sole I-BAR domain of BAIAP2 and the N-BAR domain of ARHGAP44 (Fig. 3*E*), respectively. To further quantify protein recruitment dynamics at nascent filopodial sites, we performed ratiometric image analysis at the onset of filopodia extension (*SI Appendix*, Fig. S5 *A* and *B*). For both proteins, we find a continuous increase in relative concentration starting prior to filopodial outgrowth (Fig. 3*F* and *SI Appendix*, Fig. S5*C*), which argues that protein nucleation precedes filopodial extension. Considering that kymographs and quantification were both autoscaled in order to display the relative protein kinetics, we next analyzed the absolute protein enrichment in extended filopodia. Analysis of the median protein concentration in filopodial structures 10 to 15 s after initiation showed a >10 times stronger enrichment for the negative curvature-sensing I-BAR domain compared to the N-BAR (I-BAR = +13.94%, N-BAR = +1.29%). The negative curvature-sensing I-BAR displayed a relatively uniform distribution along the filopodium, while the positive curvature-sensing N-BAR appeared to be most prominent at the base of the extending filopodium (*SI Appendix*, Fig. S5*C*). Since filopodia frequently emerge from actin patches that form along dendrites, we next probed for coenrichment of the I-BAR and N-BAR domain at such sites. To that end, we performed a cross-correlation analysis of the 100 s before filopodia extension begins (*SI Appendix*, Fig. S5*D*). We find coenrichment of positive and negative curvature sensors at minor bulging sites (i.e., actin patches) that formed along the dendrite shaft without a subsequent filopodial elongation (*SI Appendix*, Fig. S5*E*), thus further strengthening the validity of the model. Finally, we explored enrichment dynamics of I-BAR versus the BAIAP2-interacting protein VASP and versus the filamentous actin marker f-tractin. As above, we find enrichment of I-BAR/Cyto to precede filopodial extension (Fig. 3 *G* and *H*). VASP/Cyto dynamics strongly resembled I-BAR/Cyto, showing a gradual accumulation that started prior to filopodia extension (Fig. 3*G*). Actin/Cyto followed the same trend, also showing enrichment at nascent filopodial sites before extension (Fig. 3*H*).

Strikingly, the negative curvature-sensing BAIAP2 interacts with CDC42, VASP, and other proteins to promote actin polymerization and filopodia formation (18), while the positive curvature-sensitive ARHGAP44 carries a RhoGAP domain that inhibits actin polymerization and filopodial growth (40). Hence, the observed coenrichment of these proteins at nascent filopodia not only stabilizes stochastic membrane deformations but forms two interlinked actin-regulatory feedback loops (Fig. 4*A* and *SI Appendix*, *Supplementary Information Text*).

To probe the relevance of these feedback loops, we expanded the Monte Carlo model to include actin filaments that are regulated in a curvature-dependent manner (*SI Appendix*, *Supplementary Information Text*). Specifically, the filopodia were assumed to face with the barbed end toward the membrane. Polymerization only occurred if the space between the filopodia tip and the membrane was greater than half a g-actin monomer size. Similarly, the membrane only moved downward if the space between membrane and filopodia tip was greater than the simulation's spatial step size. The system exhibited a nonuniform distribution of actin filaments at the membrane and the formation of filopodial structures in the presence of I-BAR and N-BAR proteins (Fig. 4*B* and *SI Appendix*, *Supplementary Information Text*), arguing that the two interlinked actin-regulatory feedback loops further strengthen formation of stochastically formed curved membrane sections. These findings are in accordance with previous theoretical studies probing membrane dynamics in the presence of negative curvature-sensing actin promotors from our (44) and other (45, 46) groups.

Based on the wiring of this self-organizing signaling circuit, the relative strength of the competing feedback loops determines filopodial initiation probability. Notably, only the negative curvature-sensing actuator BAIAP2 responds to changes in dendrite diameter, which causes the relative weight of the competing circuit components to change along tapering neurites. Consistently, curvature-dependent increase in the BAIAP2-to-ARHGAP44 domain ratio (Fig. 4*C*) and filopodial initiation frequency show a Pearson correlation score of 0.7 (Fig. 4*D*). To directly test how circuit strength affects initiation probability, we next performed knockdown experiments. In line with the feedback model, reduced mRNA levels of Baiap2 (actuator) lowered filopodial density, whereas reduction of the *Arhgap44* (inhibitor) increased the density of filopodia along dendritic arbors (Fig. 4*E* and *SI Appendix*, Fig. S6 *A–D*). Consistent with the proposed model, knockdown-dependent changes in filopodial density were strongest at the thin distal ends (*SI Appendix*, Fig. S6*E*). Intriguingly, an e-fold (i.e., 2.718) reduction of

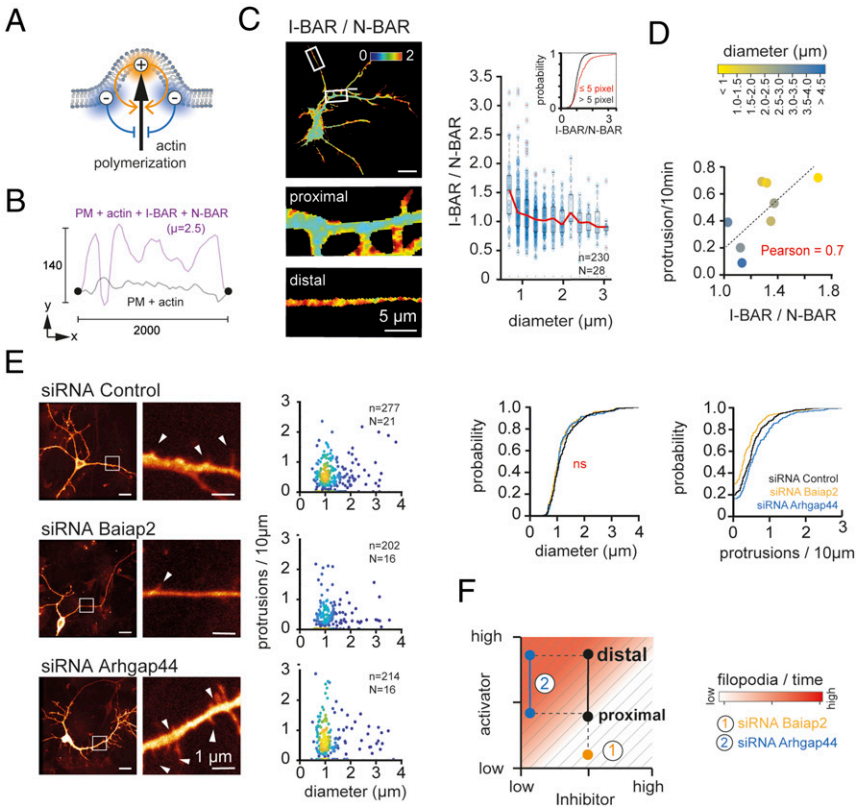

Fig. 4. Curvature-dependent self-organization mediates filopodia initiation in neurons. (*A*) Self-organizing module composed of negative curvature-sensing actuator (BAIAP2, orange) and positive curvature-sensing inhibitor (ARHGAP44, blue) controls filopodial initiation. (*B*) Monte Carlo simulation of linear membrane in the presence of curvature-dependent actin polymerization displays enhanced filopodia formation (settings: time = 300, membrane rigidity = 50, I-BAR rigidity = 35, N-BAR rigidity = 35, I-BAR curvature = -1/20, N-BAR curvature = 1/20, for I-BAR and N-BAR $\mu = 2.5$, $actin_{on} = 11.6$, $actin_{off} = 1.4$, actin concentration = 0.2412). (*C*) Dendritic tapering yields enrichment of the I-BAR domain of BAIAP2 over the N-BAR domain of ARHGAP44. Ratiometric image (*Left*) and analysis (*Right*) are shown ($n = 230$ neurites from $n = 28$ cells). (Scale bar, 5 μm.) (*D*) Filopodia initiation frequency and I-BAR/N-BAR ratio show a Pearson correlation score of +0.7. (*E*) Knockdown of *Baiap2* reduces, while siRNA directed against *Arhgap44* increases, the density of filopodia (white arrowheads) in cultured hippocampal neurons. Neurons were transfected at DIV7 with the respective siRNA and a membrane fluorescence marker and imaged 48 h later. Representative neurons (*Left*) and curvature-dependent protrusion density (next to neurons) as well as cumulative distribution of dendrite diameter (*Inner Right*) and protrusion density (*Outer Right*) are shown (siRNA *Control*: $n = 277$ neurites from $n = 21$ cells; siRNA *Baiap2*: $n = 202$ neurites from $n = 16$ cells; siRNA control: $n = 214$ neurites from $n = 16$ cells). (Scale bar, 1 μm.) (*F*) Proposed model of curvature-dependent modulation of filopodia initiation via the self-organizing module. The increase in membrane curvature from proximal to distal dendrites yields elevated actuator concentrations (*y*-axis), which augments the initiation probability of exploratory dendritic filopodia (red). Knockdown of the activator reduced the ability of the system to form exploratory filopodia (yellow), while loss of the inhibitor moves shifts the balance toward a higher activity state (blue).

actuator or inhibitor level did not prevent formation of highly curved metastable membrane sections (*SI Appendix*, Fig. S3 *C–E* and Movie S4). As stochastic membrane deformations robustly form over a wide range of protein concentrations, this argues that biased transcellular sampling along tapering dendrites is an emerging property of the self-organizing curvature-dependent signaling circuit (Fig. 4*F*).

Discussion

Here, we set out to investigate how exploratory dendritic filopodia formation is regulated in space and time. Previous work showed that ARHGAP44 expression limits exploratory dendritic filopodia (40), while BAIAP2 expression positively correlates with dendritic protrusions in cultured hippocampal neurons (18). Consistent with an exploratory role during synapse initiation, *Baiap2*$^{-/-}$ mice further display delayed synapse formation in hippocampal neurons (47). Expanding the current view, we show that in the absence of external signaling cues, membrane fluctuations cause these prototypic curvature-sensitive proteins to spontaneously assemble into a self-organizing signaling circuit that determines the initiation frequency of exploratory filopodia in developing neurons.

Conceptually, our findings yield three major conclusions. First, our data introduce a nucleation mechanism for curvature-dependent signaling hubs (*SI Appendix*, *Supplementary Information Text*). Energetic considerations demonstrate that binding of curvature-sensitive proteins to the plasma membrane stabilizes curved membrane sections. In the context of exploratory filopodia, stochastic membrane deformations were shown to coordinate actin dynamics in the proximity of a lipid bilayer and nucleate filopodial protrusions (10, 12). Hence, protein-dependent stabilization of transient membrane deformations, by itself, is prone to increase filopodial initiation probability. Second, curvature-sensitive proteins not only stabilize curved membrane sections but also regulate local actin polymerization dynamics. BAIAP2 and ARHGAP44 both contain additional protein domains that regulate actin polymerization. The resulting interlinked feedback loops, one positive and the other negative, form a self-organizing signaling circuit that controls exploratory filopodial initiation in a dosage-dependent manner. As only the actuator (i.e., BAIAP2) remains enriched in the growing filopodium, this initiation process is irreversible. How filopodial elongation is aborted upon initiation remains unclear. The observation that growth stalls upon reaching a particular length suggests that a local increase in membrane tension (48) or local actin regulation (19, 49) may contribute. Third, we find that

the dendrite diameter determines the relative protein composition of the self-organizing signaling circuit. Exploratory filopodia initiation is thus not only regulated temporally by changes in the global expression level of BAIAP2 and ARHGAP44 throughout development (40, 50) but also spatially by a concentration gradient of BAIAP2 along narrowing dendritic arbors. It remains elusive if cell-specific differences in cytoskeleton or membrane mechanics, for instance actin rings (51), alter membrane deformations and thus the ability of exploratory protrusions to form.

In summary, our studies demonstrate that transcellular sampling is an emerging property of curvature-dependent changes in actin polymerization dynamics, caused by random membrane deformations and dendritic tapering. The presented mechanism, which is purely stochastic, contrasts classical mechanisms that rely on a stimulus to trigger filopodia initiation (8, 9). We consider the proposed mechanism to work in parallel with such signal-based regulatory mechanisms to collectively regulate filopodial initiation dynamics during neuronal development. Considering that curvature preference and splice-form–specific expression profiles of curvature-sensing proteins remain largely elusive (52, 53), additional self-organizing signaling circuits are likely to partake in shaping the manifold and unique neuronal architectures present in the central nervous system.

Materials and Methods

Cell Lines and Cell Culture.

Neurons. Mouse hippocampal neurons were isolated at postnatal day 0 (P0) and plated onto sterilized glass coverslips that were previously functionalized with 70 μg/mL poly-D-lysine in bi-distilled water (ddH2O) (Sigma-Aldrich, P6407). Cultures were then incubated at 37 °C with 5% CO_2 using Neurobasal Medium (Life Technologies, 21103-049) supplemented with B27 (Life Technologies, 17504-44), 1% penicillin/streptomycin (10 U/mL; Biochrom, A12212), and 1% Glutamax (Life Technologies, 35050-061).

Immortalized cell lines. NIH 3T3 cells (DSMZ, ACC-59) and HeLa cells (DSMZ, ACC-57) were cultured in Dulbecco's Modified Eagle Medium (DMEM) supplemented with 1% Glutamax (Life Technologies, 35050-061), 10% fetal bovine serum (BioChrom AG, L11-004), and 1% penicillin/streptomycin (10 U/mL; Biochrom, A12212). C2C12 cells (LGS, ATCC-CRL-1772) were cultured in the same medium supplemented with 5% horse serum (Life Technologies, 16050-122).

Transfection and fixation. Cells were transfected using Lipofectamine 2000 (Life Technologies, 11668-027) according to the manufacturer's protocol. Fixation was accomplished using 1× phosphate buffered saline (PBS) (Gibco, 10010-02) containing 4% PFA (Sigma, P6148) and 4% Sucrose (Sigma, S7903) for 20 min at room temperature. Upon fixation, cells were washed two times with PBS and mounted with Fluoromount (Sigma-Aldrich, F4680) on glass coverslips (Engelbrecht, 11102).

Fluorescence Microscopy.

Confocal microscopy. Confocal microscopy was performed using an inverted microscope (Nikon, Eclipse Ti) equipped with a Yokogawa CSU-X1 spinning disk unit and an electron multiplying charged-coupled device EMCCD camera (Andor, IXON Ultra). Time-lapse videos and Z-stacks were acquired using a 60× objective with a binning of 1 × 1. All live-cell imaging was performed at 37 °C. For time-lapse imaging, for each channel 1,200 frames were captured at 1 Hz. In the chemical dimerization experiments, after 10 min acquisition, 100 nM rapamycin (Millipore, 553210) was added for artificial protein recruitment to the plasma membrane.

Lattice light-sheet microscopy. Lattice light-sheet microscopy was performed on a cloned setup of the original design published by Chen and colleagues (54). CFP and YFP fluorescence were excited by a 445-nm and a 488-nm laser line, respectively. Z-stacks were acquired in sample scan mode using dithered square lattice light sheets with an NA_{min} = 0.48 and NA_{max} = 0.55 and a length of 15 μm. Fluorescence was collected by a water dipping objective (Nikon, CFI Apo LWD 25XW) and imaged on a scientific complementary metal–oxide–semiconductor sCMOS detector (Hamamatsu Photonics, ORCA-Flash 4.0 V2) using a CFP/YFP/mCherry triple-band filter (Semrock, 465/537/623 HC Triple-band) and a 500-mm tube lens. Final magnification is 62.5 resulting in a pixel size of 104 nm.

TIRF and TIRF-PALM microscopy. TIRF as well as TIRF-PALM and TIRF microscopy were both performed using a Nikon CFI Apo TIRF 100× numerical aperture 1.49 oil-immersion objective on an inverted microscope (Nikon, Eclipse Ti) equipped with a CMOS camera (Hamamatsu Photonics, ORCA-Flash 4.0). For PALM acquisition, cells were illuminated at 561 nm with an effective laser power of 30 mW. Low-intensity settings were chosen for 405-nm TIRF illumination.

Scanning Electron Microscopy. Cells were fixed at DIV8-9 using 2.5% Glutaraldehyde (Agar Scientific, R1011) in 135 mM NaCacodylate buffer, pH 7.4 at 4 °C overnight. Following, cells were washed three times for 20 min in 135 mM NaCacodylate buffer, postfixed for 1 h in 1% osmium-tetraoxide (Roth, 7436.1), and again washed with buffer. Next, samples were dehydrated in an ascending ethanol series (50, 70, 80, 90, and 100%). Upon critical point drying, samples were coated with 2.5 nm platinum/carbon (Balzers, BAF300) and transferred to imaging. Neurons were imaged with a field emission scanning electron microscope (FE-SEM) Hitachi S800 using an accelerating voltage of 30 kV and a working distance of 15 mm.

Western Blot. For small interfering ribonucleic acid (siRNA) control Western blot, C2C12 cells were cotransfected with a YFP vector (Addgene, 54594) and siRNAs directed against the mRNA of *Baiap2* and *Arhgap44*, respectively. As negative control, the YFP vector was cotransfected with scrambled siRNA. For lysis, cells were first rinsed in ice-cold PBS, homogenized in ice-cold lysis buffer containing 1× radioimmunoprecipitation assay (RIPA) buffer (Cell Signaling, 9806), 1× PMSF, and a protease inhibitory mixture (Roche, 11873580001). Subsequently, cell extracts were centrifuged at 10,000 rpm for 10 min at 4 °C. Protein concentration in the supernatant was determined via Bradford Protein Assay (Biorad, 500-00006), and 20 μg lysate was loaded in the gel. Upon transfer, the relative protein levels were probed using the primary antibodies directed against BAIAP2, ARHGAP44, and TUBULIN (1:800) at 4 °C overnight. For detection, IRDye 800CW anti-rabbit (1:10,000) (LI-COR, 926-32213) and IRDye 680 anti-mouse (1:10,000) (LI-COR, 926-68070) were used.

Plasmids and Antibodies.

Plasmids. Fluorescently tagged probes for BAIAP2 (amino acids [AA] 1 to 260) (44), MTSS1 (AA 1 to 250) (44), MTSS2 (AA 1 to 260) (44), ARHGAP44 (AA 1 to 254) (40), and F-tractin (55) were previously published. Biosensors for the inverse F-BAR domain proteins SRGAP2 (AA 1 to 486) and SRGAP3 (AA 1 to 501) were generated by oligonucleotide synthesis (Gene Art Gene Synthesis, Invitrogen) and were subsequently cloned into pmCitrine-N1, pmCerulean3-N1, and pmCherry2-N1 vectors, respectively. Knockdowns were accomplished using FlexiTube siRNA directed against murine *Baiap2* and Arhgap44 mRNA (Qiagen, 1027416), while scramble control was accomplished via AllStars Neg. Control siRNA (Qiagen, 1027281). For chemical dimerization assays, the BAR domain of BAIAP2 (I-BAR) was subcloned into backbones generously provided by Dr. Takanari Inoue (Johns Hopkins University, Baltimore, MD). In these experiments, Lyn-YFP-FRB was used as membrane anchor, while the BAR domain of BAIAP2 was fused to FKBP-mCherry. Empty mCherry and CFP-tagged CAAX were used to visualize global cell shape changes. For the actin dynamics experiments, I-BAR was coexpressed with F-tractin (53) and mCherry-VASP (Addgene. 55151), respectively.

Antibodies. Primary antibodies directed against BAIAP2 (Atlas Antibodies, HPA023310), ARHGAP44 (Atlas Antibodies, HPA038814), and TUBULIN (Synaptic Systems, 302 211) were used. As secondary antibodies, we used Alexa-Fluor 488 anti-rabbit (Invitrogen, A32731), IRDye 800CW anti-rabbit (LI-COR, 926-32213), and IRDye 680 anti-mouse (LI-COR, 926-68070).

Image Analysis.

Relative protein localization in neurons. Ratiometric analysis of the protein of interest normalized to a cytosolic reference protein was performed using previously developed Matlab software that is publicly available (42, 44).

Ratiometric protein dynamics in dendritic filopodia. Analysis of protein enrichment in extending dendritic filopodia was performed using a previously developed computer vision software (42). For comparison of protein enrichment versus filopodial outgrowth, ratiometric kymographs of the protein of interest normalized to a cytosolic reference were accomplished. Following, the relative enrichment was normalized, rescaled, and the average values were plotted versus the extending filopodium.

PALM image reconstruction. Superresolution images were reconstructed using the ImageJ plug-in ThunderSTORM (56). Lateral drift was corrected using the built-in correlation algorithm, whereby pixels displaying an uncertainty >30 nm were removed before reconstruction of normalized Gaussian images. To quantitatively describe the distribution of mEos3.2-tagged BAR proteins, Voronoi tessellation of the PALM data was performed via SR-Tesseler (57). To compare the molecular density of the biosensor in neurites of different widths, we determined the number of detections obtained from individual neurites. The width of the neurite area was identified via Voronoi tessellation based on single-molecule localization data.

Statistical Analysis. Box plots span from the 25th to the 75th percentile. The center mark depicts the median. Whiskers extend to the most extreme data points not considered outliers, with outliers plotted in red using the "+" symbol. Unless stated otherwise in the figure legends, the Mann–Whitney *U* test for nonparametric data was performed for statistics. The following *P* values were used: ns (nonsignificant, $P > 0.05$), * ($P < 0.05$), ** ($P < 0.01$), *** ($P < 0.001$).

Data Availability. Matlab code data have been deposited in GitHub (https://github.com/Die-Nase/Mancinelli_2021_PNAS); Group Homepage (in progress; https://www.medizin.uni-muenster.de/impb/das-institut/zellkraefte-auf-der-nanoskala/software.html). All other study data are included in the article and/or supporting information.

ACKNOWLEDGMENTS. We thank Lukas Funke, Anastasiia Sokolova, and Katrin Tkotz for technical support. We further thank members of the M.G., Matis, and J.K. laboratories for critical feedback and discussion. M.G. acknowledges funding from the German Research Foundation (DFG) (CRC1348/A06, CRC 944/P22, GA 2268/4-1) and the Medical Faculty of the University of Münster (IZKF Ga3/016/21). J.K. acknowledges funding from the DFG (CRC1348/A02, CRC944/P5). The imaging facility Integrated Bioimaging Facility Osnabrück was funded by the DFG as a core facility (PI 405/14-1).

1. N. E. Ziv, S. J. Smith, Evidence for a role of dendritic filopodia in synaptogenesis and spine formation. *Neuron* **17**, 91–102 (1996).
2. M. E. Dailey, S. J. Smith, The dynamics of dendritic structure in developing hippocampal slices. *J. Neurosci.* **16**, 2983–2994 (1996).
3. J. C. Fiala, M. Feinberg, V. Popov, K. M. Harris, Synaptogenesis via dendritic filopodia in developing hippocampal area CA1. *J. Neurosci.* **18**, 8900–8911 (1998).
4. S. Ebrahimi, S. Okabe, Structural dynamics of dendritic spines: Molecular composition, geometry and functional regulation. *Biochim. Biophys. Acta* **1838**, 2391–2398 (2014).
5. P. Hotulainen, C. C. Hoogenraad, Actin in dendritic spines: Connecting dynamics to function. *J. Cell Biol.* **189**, 619–629 (2010).
6. J. de Wit, A. Ghosh, Specification of synaptic connectivity by cell surface interactions. *Nat. Rev. Neurosci.* **17**, 22–35 (2016).
7. W. Hou *et al.*, The actin nucleator Cobl is controlled by calcium and calmodulin. *PLoS Biol.* **13**, e1002233 (2015).
8. A. Disanza *et al.*, CDC42 switches IRSp53 from inhibition of actin growth to elongation by clustering of VASP. *EMBO J.* **32**, 2735–2750 (2013).
9. H.-B. Kwon, B. L. Sabatini, Glutamate induces de novo growth of functional spines in developing cortex. *Nature* **474**, 100–104 (2011).
10. C. Simon *et al.*, Actin dynamics drive cell-like membrane deformation. *Nat. Phys.* **15**, 602–609 (2019).
11. K. Lee, J. L. Gallop, K. Rambani, M. W. Kirschner, Self-assembly of filopodia-like structures on supported lipid bilayers. *Science* **329**, 1341–1345 (2010).
12. A. P. Liu *et al.*, Membrane-induced bundling of actin filaments. *Nat. Phys.* **4**, 789–793 (2008).
13. T. M. Svitkina *et al.*, Mechanism of filopodia initiation by reorganization of a dendritic network. *J. Cell Biol.* **160**, 409–421 (2003).
14. P. Hotulainen *et al.*, Defining mechanisms of actin polymerization and depolymerization during dendritic spine morphogenesis. *J. Cell Biol.* **185**, 323–339 (2009).
15. C. Portera-Cailliau, D. T. Pan, R. Yuste, Activity-regulated dynamic behavior of early dendritic protrusions: Evidence for different types of dendritic filopodia. *J. Neurosci.* **23**, 7129–7142 (2003).
16. J. Saarikangas *et al.*, MIM-induced membrane bending promotes dendritic spine initiation. *Dev. Cell* **33**, 644–659 (2015).
17. C. Chatzi *et al.*, Exercise-induced enhancement of synaptic function triggered by the inverse BAR protein, Mtss1L. *eLife* **8**, 8 (2019).
18. J. Choi *et al.*, Regulation of dendritic spine morphogenesis by insulin receptor substrate 53, a downstream effector of Rac1 and Cdc42 small GTPases. *J. Neurosci.* **25**, 869–879 (2005).
19. K. Kawabata Galbraith *et al.*, MTSS1 regulation of actin-nucleating formin DAAM1 in dendritic filopodia determines final dendritic configuration of Purkinje cells. *Cell Rep.* **24**, 95–106.e9 (2018).
20. H. Nakagawa *et al.*, IRSp53 is colocalised with WAVE2 at the tips of protruding lamellipodia and filopodia independently of Mena. *J. Cell Sci.* **116**, 2577–2583 (2003).
21. J. Saarikangas *et al.*, ABBA regulates plasma-membrane and actin dynamics to promote radial glia extension. *J. Cell Sci.* **121**, 1444–1454 (2008).
22. H. Miki, H. Yamaguchi, S. Suetsugu, T. Takenawa, IRSp53 is an essential intermediate between Rac and WAVE in the regulation of membrane ruffling. *Nature* **408**, 732–735 (2000).
23. K. D. Mertz *et al.*, MTSS1 is a metastasis driver in a subset of human melanomas. *Nat. Commun.* **5**, 3465 (2014).
24. E. S. Lein *et al.*, Genome-wide atlas of gene expression in the adult mouse brain. *Nature* **445**, 168–176 (2007).
25. C. Prévost *et al.*, IRSp53 senses negative membrane curvature and phase separates along membrane tubules. *Nat. Commun.* **6**, 8529 (2015).
26. D. J. Kast *et al.*, Mechanism of IRSp53 inhibition and combinatorial activation by Cdc42 and downstream effectors. *Nat. Struct. Mol. Biol.* **21**, 413–422 (2014).
27. A. Pykäläinen *et al.*, Pinkbar is an epithelial-specific BAR domain protein that generates planar membrane structures. *Nat. Struct. Mol. Biol.* **18**, 902–907 (2011).
28. P. J. Carman, R. Dominguez, BAR domain proteins-a linkage between cellular membranes, signaling pathways, and the actin cytoskeleton. *Biophys. Rev.* **10**, 1587–1604 (2018).
29. A. S. Kim, L. T. Kakalis, N. Abdul-Manan, G. A. Liu, M. K. Rosen, Autoinhibition and activation mechanisms of the Wiskott–Aldrich syndrome protein. *Nature* **404**, 151–158 (2000).
30. A. M. Lebensohn, M. W. Kirschner, Activation of the WAVE complex by coincident signals controls actin assembly. *Mol. Cell* **36**, 512–524 (2009).
31. T. Inoue, W. D. Heo, J. S. Grimley, T. J. Wandless, T. Meyer, An inducible translocation strategy to rapidly activate and inhibit small GTPase signaling pathways. *Nat. Methods* **2**, 415–418 (2005).
32. A. Suarez, T. Ueno, R. Huebner, J. M. McCaffery, T. Inoue, Bin/Amphiphysin/Rvs (BAR) family members bend membranes in cells. *Sci. Rep.* **4**, 4693 (2014).
33. M. Maletic-Savatic, R. Malinow, K. Svoboda, Rapid dendritic morphogenesis in CA1 hippocampal dendrites induced by synaptic activity. *Science* **283**, 1923–1927 (1999).
34. W. Helfrich, Elastic properties of lipid bilayers: Theory and possible experiments. *Z. Naturforsch. C* **28**, 693–703 (1973).
35. T. Baumgart, S. T. Hess, W. W. Webb, Imaging coexisting fluid domains in biomembrane models coupling curvature and line tension. *Nature* **425**, 821–824 (2003).
36. T. V. S. Krishnan, S. L. Das, P. B. S. Kumar, Models for membrane curvature sensing of curvature generating proteins. *Pramana* **94**, 590 (2020).
37. A. Breuer, L. Lauritsen, E. Bertseva, I. Vonkova, D. Stamou, Quantitative investigation of negative membrane curvature sensing and generation by I-BARs in filopodia of living cells. *Soft Matter* **15**, 9829–9839 (2019).
38. P. K. Mattila *et al.*, Missing-in-metastasis and IRSp53 deform PI(4,5)P2-rich membranes by an inverse BAR domain-like mechanism. *J. Cell Biol.* **176**, 953–964 (2007).
39. S. Ramaswamy, J. Toner, J. Prost, Nonequilibrium fluctuations, traveling waves, and instabilities in active membranes. *Phys. Rev. Lett.* **84**, 3494–3497 (2000).
40. M. Galic *et al.*, Dynamic recruitment of the curvature-sensitive protein ArhGAP44 to nanoscale membrane deformations limits exploratory filopodia initiation in neurons. *eLife* **3**, e03116 (2014).
41. C. Monzel, K. Sengupta, Measuring shape fluctuations in biological membranes. *J. Phys. D Appl. Phys.* **49**, 243002 (2016).
42. T. Saha *et al.*, Automated analysis of filopodial length and spatially resolved protein concentration via adaptive shape tracking. *Mol. Biol. Cell* **27**, 3616–3626 (2016).
43. A. Mogilner, B. Rubinstein, The physics of filopodial protrusion. *Biophys. J.* **89**, 782–795 (2005).
44. I. Begemann *et al.*, Mechanochemical self-organization determines search pattern in migratory cells. *Nat. Phys.* **15**, 848–857 (2019).
45. M. Fošnarič *et al.*, Theoretical study of vesicle shapes driven by coupling curved proteins and active cytoskeletal forces. *Soft Matter* **15**, 5319–5330 (2019).
46. N. S. Gov, A. Gopinathan, Dynamics of membranes driven by actin polymerization. *Biophys. J.* **90**, 454–469 (2006).
47. C. Sawallisch *et al.*, The insulin receptor substrate of 53 kDa (IRSp53) limits hippocampal synaptic plasticity. *J. Biol. Chem.* **284**, 9225–9236 (2009).
48. Z. Shi, Z. T. Graber, T. Baumgart, H. A. Stone, A. E. Cohen, Cell membranes resist flow. *Cell* **175**, 1769–1779.e13 (2018).
49. J. Funk *et al.*, Profilin and formin constitute a pacemaker system for robust actin filament growth. *eLife* **8**, 8 (2019).
50. C.-J. Chen *et al.*, SH2B1 and IRSp53 proteins promote the formation of dendrites and dendritic branches. *J. Biol. Chem.* **290**, 6010–6021 (2015).
51. K. Xu, G. Zhong, X. Zhuang, Actin, spectrin, and associated proteins form a periodic cytoskeletal structure in axons. *Science* **339**, 452–456 (2013).
52. J. Kang, H. Park, E. Kim, IRSp53/BAIAP2 in dendritic spine development, NMDA receptor regulation, and psychiatric disorders. *Neuropharmacology* **100**, 27–39 (2016).
53. T. Sistig *et al.*, Mtss1 promotes maturation and maintenance of cerebellar neurons via splice variant-specific effects. *Brain Struct. Funct.* **222**, 2787–2805 (2017).
54. B.-C. Chen *et al.*, Lattice light-sheet microscopy: Imaging molecules to embryos at high spatiotemporal resolution. *Science* **346**, 1257998 (2014).
55. H. W. Johnson, M. J. Schell, Neuronal IP3 3-kinase is an F-actin-bundling protein: Role in dendritic targeting and regulation of spine morphology. *Mol. Biol. Cell* **20**, 5166–5180 (2009).
56. M. Ovesný, P. Křížek, J. Borkovec, Z. Svindrych, G. M. Hagen, ThunderSTORM: A comprehensive ImageJ plug-in for PALM and STORM data analysis and super-resolution imaging. *Bioinformatics* **30**, 2389–2390 (2014).
57. F. Levet *et al.*, SR-Tesseler: A method to segment and quantify localization-based super-resolution microscopy data. *Nat. Methods* **12**, 1065–1071 (2015).